

# Covariance Symmetries Classification in Multitemporal/Multipass PolSAR Images

Dehbia Hanis<sup>1</sup>, Luca Pallotta<sup>1</sup>, *Senior Member, IEEE*, Augusto Aubry<sup>2</sup>, *Senior Member, IEEE*, Aichouche Belhadj-Aissa<sup>3</sup>, and Antonio De Maio<sup>4</sup>, *Fellow, IEEE*

**Abstract**—A polarimetric synthetic aperture radar (PolSAR) system, which uses multiple images acquired with different polarizations in both transmission and reception, has the potential to improve the description and interpretation of the observed scene. This is typically achieved by exploiting the polarimetric covariance or coherence matrix associated with each pixel, which is processed to meet a specific goal in Earth observation. This paper presents a design framework for selecting the structure of the polarimetric covariance matrix that accurately reflects the symmetry associated with the analyzed pixels. The proposed methodology leverages both polarimetric and temporal information from multipass PolSAR images to enhance the retrieval of information from the acquired data. To accomplish this, it is assumed that the covariance matrix (of the overall acquired data) is given as the Kronecker product of the temporal and polarimetric covariances. An alternating maximization algorithm, known as the flip-flop method, is then developed to estimate both matrices while enforcing the symmetry constraint on the polarimetric covariance. Subsequently, the symmetry structure classification is formulated as a multiple hypothesis testing problem, which is solved using model order selection techniques. The proposed approach is quantitatively assessed on simulated data, showing its advantages over its competitor, which does not exploit temporal correlations. For example, it reaches accuracies of 94.6% and 92.0% for the reflection and azimuth symmetry classes, respectively, while the competitor achieves 72.5% and 72.6% under the same simulation conditions. Moreover, the proposed method can realize a Cohen's kappa coefficient of 0.95, which significantly exceeds that of its counterpart equal to 0.78. Finally, the effectiveness of the proposed framework is further demonstrated using measured RADARSAT-2 data, corroborating the results obtained from the simulations. Specifically, tests conducted applying the Freeman-Durden Wishart classification have proved that the new approach greatly enhances the accuracy of pixel classification. For instance, in areas dominated by surface scattering, it boosts the percentage of correctly classified pixels from 68.23%, achieved using the classic method, to 91.65%.

**Index Terms**—land cover classification, model order selection (MOS) rules, multitemporal PolSAR images, polarimetric coher-

ence and covariance matrix, polarimetric SAR.

## I. INTRODUCTION

MODERN polarimetric synthetic aperture radar (PolSAR) systems that use multiple images acquired with distinct polarizations in both transmission and reception have the potential to improve the description and interpretation of the observed scene (including enhancements in the classification, detection and/or recognition capabilities of the entire system) [1]. This process typically involves statistical inference from the data corresponding to individual pixels that can be gathered via appropriate probing schemes [1], [2]. In this context, the polarimetric covariance (or coherence) matrix is one of the primary tools used to infer the scattering mechanisms that characterize the observed objects of the analyzed scenario. The polarimetric covariance matrix contains hidden information that can help differentiating various aspects in the SAR image. This includes distinguishing between different areas, such as land versus sea, bare fields versus cultivated ones, or buildings versus trees. It also allows for the discrimination between categories within the same type, like small-stem crops versus broad-leaf crops, as well as identifying different scattering mechanisms, such as dipole, diplane, and trihedral. In this respect, several polarimetric decompositions based on coherence matrix [3]–[7] aid in identifying different scattering mechanisms like surface, volume, and double-bounce scattering. The interested reader may also refer to [8]–[10] for further approaches. Additionally, several strategies for scene classification/segmentation (typically categorized into unsupervised or supervised algorithms) exploiting the polarimetric information in SAR images can be found, for instance, in [11]–[22]. The unsupervised method involves grouping image pixels based on shared characteristics or features, and operates automatically without user intervention. On the other hand, the supervised method necessitates user involvement, where algorithms are trained using pre-classified reference samples to classify new, unknown data. For instance, in [11], both amplitude and phase information from the polarimetric channels are used to distinguish different scattering behaviors, allowing the interpretation of radar images in terms of surface characterization of various types of terrain. Analogously in [16], the authors propose a new model for vegetation scattering mechanisms in mountainous forests, extending the classic radiative transfer model by accounting for the sloping ground surface beneath the vegetation canopy.

arXiv:2505.11137v1 [eess.SP] 16 May 2025

Manuscript received September 13, 2024. This research activity of Dehbia Hanis has been conducted during her visit at University of Basilicata, under the local scientific supervision of Dr. Luca Pallotta.

(Corresponding author: Antonio De Maio.)

D. Hanis, and A. Belhadj-Aissa are with the Laboratory of Image Processing and Radiation, University of Sciences and Technology Houari Boumediene (USTHB), Algiers, Algeria. E-mail: dehbia\_hanis@yahoo.com, houria.belhadjaissa@gmail.com.

L. Pallotta is with Department of Engineering (DiING), University of Basilicata, via dell'Ateneo Lucano 10, 85100 Potenza, Italy. E-mail: luca.pallotta@unibas.it.

A. Aubry and A. De Maio are with the Department of Electrical Engineering and Information Technology (DIETI), Università degli Studi di Napoli "Federico II", via Claudio 21, I-80125 Napoli, Italy, and with National Inter-University Consortium for Telecommunications (CNIT), Parma, Italy. E-mail: {augusto.aubry, ademaio}@unina.it.

Most of the above analyses rely on second-order moment-based metrics, namely the covariance and coherence matrices, which are object of an estimation process. Often, the covariance matrix is obtained as the sample covariance matrix (SCM) which is its maximum likelihood (ML) estimate assuming a homogeneous environment (i.e., zero-mean independent and identically distributed (i.i.d.) circularly symmetric Gaussian data). This involves taking the outer product of the observation vector with its Hermitian transpose and then spatial averaging over a large enough window of pixels to get the overall SCM. Unfortunately, the SCM suffers from some limitations, such as the scarcity of homogeneous data that can be extracted from the spatial neighborhood of the pixel under test. As a consequence, before applying any of the above decompositions, more sophisticated covariance estimators can be used in place of the SCM to exploit intrinsic characteristics of the observed scene. In particular, the polarimetric covariance matrix may exhibit a distinct structure when significant scattering symmetry features (i.e., reflection symmetry, rotation symmetry, and azimuth symmetry) dominate the radar return [7], [23]. Hence, it becomes crucial to establish the presence of specific symmetries as a preliminary stage for image processing interpretation. In fact, by examining these symmetries, it can be gained insight into the physical properties and nature (e.g., vegetation, water bodies, urban areas) of SAR backscatters in the observed region. Notably, enforcing symmetry in the estimation process allows for better exploitation of the underlying scattering mechanisms for classification purposes. Moreover, since fewer parameters need to be estimated, fewer looks are required, making the process less sensitive to spatial variability of the parameters. In such a context, in [24], [25], a PolSAR covariance symmetries detection framework has been proposed and analyzed. The problem has been framed as a multiple hypothesis testing task involving nested instances (the four hypotheses refer to absence of symmetry, reflection symmetry, rotation symmetry, and azimuth symmetry [7], [23]), and several model order selection (MOS) criteria [26]–[29] have been applied to classify each pixel according to its respective covariance structure. The core objective of the MOS rules is to minimize the Kullback-Leibler divergence between the proposed set of candidate models and the actual data distribution [26]–[29]. In fact, they address the limitations of the generalized maximum likelihood (GML) method [30], [31] by incorporating a penalty term, which accounts for the number of unknown parameters, into the likelihood function for each hypothesis prior to its maximization. This is necessary because the GML fails completely in the presence of nested hypotheses, resulting in the selection of the instance that encompasses all others. It is also worth underlining that the polarimetric covariance structure classification framework in [24] has been also extended to account for data heterogeneity [32], when data are filtered before performing inferences [33], [34], as well as assuming that the pixels in the extracted neighborhood do not share the same symmetry [35].

This paper for the first time introduces a methodology for the automatic classification of the symmetric structure of the polarimetric covariance matrix in multipass/multitemporal PolSAR imagery. The approach aims to enhance the estimation

of pixel polarimetric characteristics by processing multiple observations of the same scene while accounting for temporal correlation. This establishes a comprehensive framework that extends beyond the single-image symmetry detection method outlined in [24], by jointly processing all available multi-temporal acquisitions, and hence exploiting the additional information arising from observing more than one image of the same scene. In particular, the data are modeled as Gaussian-distributed, where the covariance matrix is expressed as the Kronecker product of temporal and polarimetric covariance matrices. The polarimetric component is constrained to conform to the specific symmetry properties above described, while the temporal covariance is assumed to be positive definite but unstructured. In addressing the resulting problem, the estimate of the Kronecker-structured temporal/polarimetric covariance matrix is derived using a *flip-flop* algorithm, which alternates between estimating the temporal and polarimetric covariances while enforcing the symmetry structures, and ensuring its convergence to a stationary point of the design optimization problem. Notice that, for the case of absence of symmetry (e.g., for both temporal and polarimetric unstructured matrices), the covariance estimate can be obtained as the solution of the flip-flop (or *ping-pong*) algorithm in [36]. Subsequently, to accurately select the polarimetric structure that best represents the dominant symmetry of the pixels' return, several MOS criteria are synthesized. They integrate the ML estimates of the covariance structures identified in the previous stage. Extensive simulations are conducted to quantitatively demonstrate the effectiveness of the developed strategy, also with respect to its competitor. Finally, the devised procedure is also validated on a pair of real-recorded PolSAR images from RADARSAT-2. To facilitate the reader's understanding, it is important to disclose here that the innovations introduced by the proposed framework can be summarized in the following steps:

- 1) introduction of a bespoke model for structured covariance matrix estimation in the presence of multiple polarimetric SAR acquisitions;
- 2) design of a *flip-flop* based algorithm for the estimation of the (unstructured) temporal and (structured) polarimetric covariance matrices;
- 3) synthesis of MOS rules for selecting the correct hypothesis in terms of covariance structure;
- 4) extensive simulations and tests on real-recorded data.

The remainder of the paper is structured as follows: Section II describes the process for multipass datacube formation, while Section III summarizes the covariance matrices under the different symmetries' hypothesis. In Section IV the estimation and classification problems are formulated, and the solution for the Kronecker structured covariance estimate is developed. Then, Section V presents the proposed framework for polarimetric covariance symmetries classification. The performance of the devised technique applied on simulated and real X-band SAR data is presented and discussed in Section VI. Finally, some concluding remarks are given in Section VII.

## NOTATION

Boldface is used for vectors  $\mathbf{a}$  (lower case), and matrices  $\mathbf{A}$  (upper case). The conjugate and conjugate transpose operators are denoted by the symbols  $(\cdot)^*$  and  $(\cdot)^H$  respectively, whereas the symbol  $(\cdot)^{-1}$  denotes the inverse.  $\text{tr}\{\cdot\}$  and  $|\cdot|$  are respectively the trace and the determinant of the square matrix argument.  $\mathbf{I}$  and  $\mathbf{0}$  denote respectively the identity matrix and the matrix with zero entries (their size is determined from the context). The vector  $\text{vec}\{\cdot\}$  is obtained by stacking the columns of its matrix argument on top of each other.  $\text{diag}(\mathbf{a})$  indicates the diagonal matrix whose  $i$ -th diagonal element is the  $i$ -th entry of  $\mathbf{a}$ . The letter  $j$  represents the imaginary unit (i.e.  $j = \sqrt{-1}$ ). For any complex number  $x$ ,  $|x|$  represents the modulus of  $x$ ,  $\text{Re}\{x\}$  is its real part, and  $\text{Im}\{x\}$  is its imaginary part. Moreover,  $\mathcal{H}_n^{++}$  is the set of  $n \times n$  positive semi-definite (psd) Hermitian matrices,  $\mathcal{S}_n^{++}$  is the set of  $n \times n$  psd symmetric matrices, and  $\mathcal{P}_n^{++}$  is the set of  $n \times n$  real psd persymmetric matrices. A real persymmetric matrix  $\mathbf{C}_n$  is a matrix with the following property  $\mathbf{C}_n = \mathbf{J}\mathbf{C}_n^T\mathbf{J}$ , with  $\mathbf{J}$  the  $n \times n$  permutation matrix

$$\mathbf{J} = \begin{bmatrix} 0 & 0 & \cdots & 0 & 1 \\ 0 & 0 & \cdots & 1 & 0 \\ \vdots & \vdots & & \vdots & \vdots \\ 0 & 1 & \cdots & 0 & 0 \\ 1 & 0 & \cdots & 0 & 0 \end{bmatrix}.$$

The symbols  $\otimes$  and  $\odot$  indicate the Kronecker and the element-wise or Hadamard product, respectively. Finally,  $\mathbb{E}[\cdot]$  denotes statistical expectation.

## II. MULTIPASS DATACUBE DEFINITION

A PolSAR system collects  $N = 4$  complex returns for each observed image pixel, leveraging four different polarimetric channels, viz., HH, HV, VH, and VV. Generally, the number of polarimetric returns is reduced to  $N = 3$  since the reciprocity theorem is assumed valid [37], [38] and the HV and VH channels are substituted by their coherent average [39], namely  $(\text{HV} + \text{VH})/2$ , or a single cross-polarimetric channel is used.

With reference to the case  $N = 3$ , the polarimetric returns regarding the same pixel are hence organized in the vector  $\mathbf{y} = [y_{\text{HH}}, y_{\text{HV}}, y_{\text{VV}}]^T$ , where  $y_{tr}$  denotes the complex polarimetric return in the transmitting and receiving polarization  $t \in \{\text{H}, \text{V}\}$  and  $r \in \{\text{H}, \text{V}\}$ , respectively. As a consequence, denoting by  $L$  and  $C$  the vertical and horizontal size of the image, respectively, a datacube  $\mathbf{Y}$ , composed by the vectors  $\mathbf{Y}(c, l)$ ,  $l = 1, \dots, L$ ,  $c = 1, \dots, C$ , each of size  $N$  is formed. Therefore, the sensor provides a 3-D data stack  $\mathbf{Y}$  of size  $L \times C \times N$  which is referred to as datacube in the following.

Now, in the presence of multiple observations (repeated passes) of the same scene, let us now consider the availability of  $M$  datacubes,  $\mathbf{Y}_m$ ,  $m = 1, \dots, M$ , each of them associated with the acquisition of a PolSAR image representing the same scene. In the following, it is assumed that the  $M$  PolSAR images are already registered to each other. The formation process of the PolSAR datacubes is hence described through a graphical representation in Figure 1.

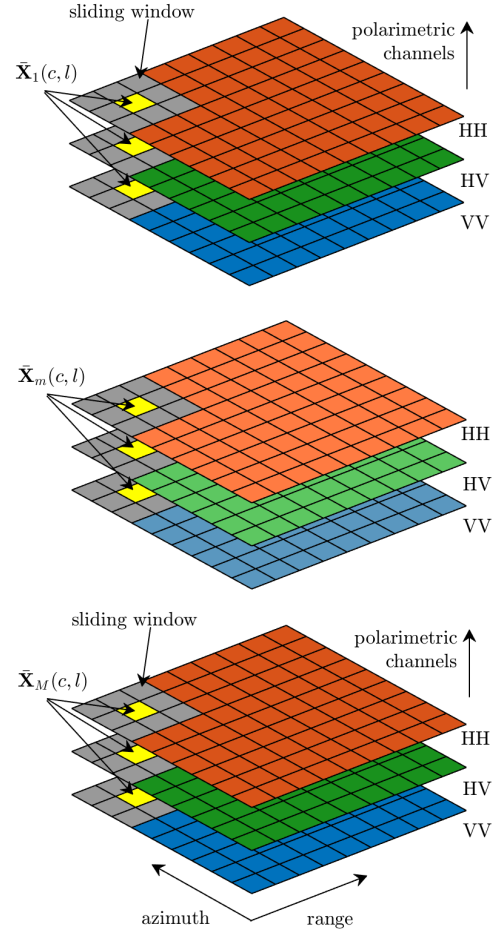


Figure 1: A visual representation depicting the structure of the multipass PolSAR datacube, comprising  $M$  PolSAR datacubes.

Now, for each pixel under test, a rectangular neighborhood  $\mathcal{A}$  of size  $K = W_1 \times W_2$  is extracted, and the matrix whose columns are the vectors of the polarimetric returns from the pixels of  $\mathbf{Y}_m$ ,  $m = 1, \dots, M$ , which fall in the region  $\mathcal{A}$  is denoted by  $\bar{\mathbf{X}}_m$ ,  $m = 1, \dots, M$ . Let us also indicate with  $\mathbf{X}$  the multipass datacube obtained stacking together all single datacubes  $\bar{\mathbf{X}}_m$ ,  $m = 1, \dots, M$ , such that the information from a given pixel are collected along a specific column of  $\mathbf{X}$ . Specifically, the pixels with the same coordinates are aligned to each other. Hence, the vectors contained in the sliding window centered on the pixel of interest are  $\mathbf{x}_1, \mathbf{x}_2, \dots, \mathbf{x}_K$ . In particular, each polarimetric vector  $\mathbf{x}_k$ ,  $k = 1, \dots, K$  is obtained stacking the different vectors obtained in the  $M$  passes. This implies that the size of each vector  $\mathbf{x}_k$ ,  $k = 1, \dots, K$ , is equal to  $3M$ .

## III. BACKGROUND ON POLARIMETRIC COVARIANCE SYMMETRIES

This section describes the polarimetric covariance matrix structures that arise when significant scattering symmetric properties [7, pp. 69-72], [23] dominate the return associated

with the pixel under investigation. They are distinguished in absence of symmetry, reflection symmetry, rotation symmetry, and azimuth symmetry [23], whose structures are detailed in what follows.

The first considered structure examines the polarimetric covariance matrix in the presence of a reciprocal medium [7], [23], which is a  $3 \times 3$  Hermitian matrix of the form

$$\mathbf{C}_p = \begin{bmatrix} c_{hhhh} & c_{hhhv} & c_{hhvv} \\ c_{hhhv}^* & c_{hvvv} & c_{hvvv} \\ c_{hhvv}^* & c_{hvvv}^* & c_{vvvv} \end{bmatrix}. \quad (1)$$

This matrix depends on  $\zeta_p = 9$  real-valued scalar quantities. In fact, its diagonal entries are the conventional (real-valued) backscattering coefficients, whereas the off-diagonal elements are complex.

The next structure is a reflection symmetry relative to a vertical plane. It is usually observed over horizontal natural environments and produces complete decorrelations between co-polarized and cross-polarized elements [23]. Under reflection symmetry, the covariance matrix has a special form ruled by  $\zeta_p = 5$  real scalar values, that is

$$\mathbf{C}_p = \begin{bmatrix} c_{hhhh} & 0 & c_{hhvv} \\ 0 & c_{hvhh} & 0 \\ c_{hhvv}^* & 0 & c_{vvvv} \end{bmatrix}. \quad (2)$$

Reflection symmetry can be observed, for instance, on water surfaces, in plowed fields, as well as in natural environments like forests, snow-covered areas, or sea ice. Additionally, this symmetry can be seen in structures like horizontal and vertical wires, or horizontal dihedrals [7], [23], [25].

Let us now consider the case of rotation symmetry [23]. Under this assumption, the polarimetric covariance matrix assumes the following special structure

$$\mathbf{C}_p = \begin{bmatrix} c_{hhhh} & c_{hhhv} & c_{hhvv} \\ -c_{hhhv} & c_{hvhh} & c_{hhvv} \\ c_{hhvv} & -c_{hhhv} & c_{hhhh} \end{bmatrix}, \quad (3)$$

with  $c_{hhhv}$  purely imaginary,  $c_{hhvv}$  purely real, and  $c_{hvhh} = (c_{hhhh} - c_{hhvv})/2$ . Under rotation symmetry, the covariance is hence described by  $\zeta_p = 3$  real scalar values. Rotation symmetry could be observed in forest canopy with helical structures in the vegetation (e.g., highly random vegetation) [7], [23], [25], [40].

The last considered symmetry, typically referred to as azimuth symmetry, is a combination of a rotation and a reflection symmetry [23]. The polarimetric covariance matrix can be constructed from  $\zeta_p = 2$  real scalar values and has the form

$$\mathbf{C}_p = \begin{bmatrix} c_{hhhh} & 0 & c_{hhvv} \\ 0 & c_{hvhh} & 0 \\ c_{hhvv} & 0 & c_{hhhh} \end{bmatrix}, \quad (4)$$

with  $c_{hvhh} = (c_{hhhh} - c_{hhvv})/2$ . An example of azimuth symmetry can be seen in vegetated areas at low frequencies and normal incidence, where the electromagnetic wave penetrates the foliage canopy and is scattered back by the horizontal branches or vertical tree trunks [7], [23], [25].

In what follows,  $\mathcal{P}_i^S$ ,  $i = 1, \dots, 4$ , is used to denote the sets of the above defined structured covariance matrices.

#### IV. PROBLEM FORMULATION AND PROPOSED SOLUTION

The polarimetric acquisitions of the same scene at different times may show total or partial decorrelation. This can happen due to changes in the object's geometry and its variability over time, as well as system decorrelation. Generally, the noise system is assumed negligible in the devised models, hence the available SAR images are acquired with high signal-to-noise ratio (SNR), and the decorrelation becomes a defining characteristic of the observed object only. Hence, in the following, multitemporal polarimetric information is properly exploited to effectively characterize the observed scene or objects in it contained.

Let us hence consider the availability of  $K$  multitemporal polarimetric data  $\mathbf{x}_k$ ,  $k = 1, \dots, K$ , modelled as statistically i.i.d. complex circular zero-mean Gaussian vectors with positive definite covariance matrix  $\mathbf{C} = \mathbf{C}_t \otimes \mathbf{C}_p$ , namely

$$\mathbf{x}_k \sim \mathcal{CN}(0, \mathbf{C}_t \otimes \mathbf{C}_p), \quad (5)$$

where  $\mathbf{C}_t$  is the  $M \times M$  (unstructured) temporal covariance matrix related to multipass acquisitions, whereas  $\mathbf{C}_p$  is the  $3 \times 3$  polarimetric covariance matrix that can exhibit one among the different structures described in Section III.<sup>1</sup>

Before proceeding further, let us discuss the reason behind the choice of this particular covariance structure. When dealing with high-dimensional covariances of multivariate phenomena, using Kronecker product decompositions allows estimating (lower-dimensional) covariances for each dimension [36]. This Kronecker structure arises when the correlation function between two distinct groups of 2D (time and polarization) data can be factorized to separately represent intra-group and inter-group correlations [41].

Let us now focus on the probability density function (pdf) of the observable matrix  $\mathbf{X}$  [36]

$$f_{\mathbf{X}}(\mathbf{X}|\mathbf{C}) = \frac{1}{\pi^{NMK} |\mathbf{C}|^K} \exp \left\{ -\text{tr} \left( \mathbf{C}^{-1} \mathbf{X} \mathbf{X}^H \right) \right\}, \quad (6)$$

and denote by

$$\hat{\mathbf{S}} = \frac{1}{K} \mathbf{X} \mathbf{X}^H = \frac{1}{K} \sum_{k=1}^K \mathbf{x}_k \mathbf{x}_k^H, \quad (7)$$

the SCM. The corresponding negative log-likelihood function of  $\mathbf{X}$  can also be derived as

$$l(\mathbf{C}; \mathbf{X}) = K \log |\mathbf{C}| + K \text{tr} \{ \hat{\mathbf{S}} \mathbf{C}^{-1} \} + NMK \log(\pi). \quad (8)$$

Hence, assuming a specific structure for the polarimetric covariance, the ML estimate of the covariance matrix  $\mathbf{C}$  can be obtained as the optimal solution to the following optimization problem under the constraints  $\mathbf{C} = \mathbf{C}_t \otimes \mathbf{C}_p$ ,  $\mathbf{C}_t \in \mathcal{H}_M^{++}$ , and  $\mathbf{C}_p \in \mathcal{P}_i^S \cap \mathcal{H}_N^{++}$ ,  $i = 1, \dots, 4$ , namely

<sup>1</sup>Notice that, the polarimetric matrix refers to the covariance (also known as coherency information) of polarimetric data gathered in a given acquisition (in time and space), modeling the scattering properties of the target, whereas, the temporal matrix accounts for the statistical dependency of the temporal data acquired in a given channel, and models the time-domain dynamics of the observed scene.

$$\begin{cases} \min_{\mathbf{C}} & l(\mathbf{C}; \mathbf{X}) \\ \text{s.t.} & \mathbf{C} = \mathbf{C}_t \otimes \mathbf{C}_p \\ & \mathbf{C}_t \in \mathcal{H}_M^{++} \\ & \mathbf{C}_p \in \mathcal{P}_i^S \cap \mathcal{H}_N^{++}, i = 1, \dots, 4 \end{cases} \quad (9)$$

or equivalently

$$\begin{cases} \min_{\mathbf{C}} & \log |\mathbf{C}| + \text{tr} \{ \hat{\mathbf{S}} \mathbf{C}^{-1} \} \\ \text{s.t.} & \mathbf{C} = \mathbf{C}_t \otimes \mathbf{C}_p \\ & \mathbf{C}_t \in \mathcal{H}_M^{++} \\ & \mathbf{C}_p \in \mathcal{P}_i^S \cap \mathcal{H}_N^{++}, i = 1, \dots, 4 \end{cases} \quad (10)$$

When a structure is imposed on the covariance matrices in addition to being Hermitian (as for instance the Kronecker structure), the optimization problem in (10) cannot in general be solved in closed form. As a consequence, its solution (leading to an estimate of the two covariances  $\mathbf{C}_t$  and  $\mathbf{C}_p$ ) can be approached, with some guarantee of optimality, through an iterative alternating minimization algorithm (a.k.a. flip-flop or ping-pong) [36]. As a matter of fact, it involves alternating minimization with respect to  $\mathbf{C}_t$  and  $\mathbf{C}_p$ , while keeping the most recent estimate of  $\mathbf{C}_t$  fixed when minimizing over  $\mathbf{C}_p$  and viceversa [36].

To this end, let us recall some useful properties related to the Kronecker product of matrices. Knowing the relationship between the determinant of the Kronecker product  $\mathbf{C}_t \otimes \mathbf{C}_p$  and the determinants of the matrices  $\mathbf{C}_t$  and  $\mathbf{C}_p$  is given by

$$|\mathbf{C}_t \otimes \mathbf{C}_p| = |\mathbf{C}_t|^M \cdot |\mathbf{C}_p|^N$$

Exploiting the above result, the objective function in (10) can be recast as

$$l(\mathbf{C}_t, \mathbf{C}_p; \mathbf{X}) = M \log |\mathbf{C}_t| + N \log |\mathbf{C}_p| + \text{tr} \left\{ \hat{\mathbf{S}} (\mathbf{C}_t^{-1} \otimes \mathbf{C}_p^{-1}) \right\}. \quad (11)$$

**Optimization over  $\mathbf{C}_p$ .** For a fixed  $\mathbf{C}_t$ , the ML estimate of  $\mathbf{C}_p$  can be obtained by minimizing (11) while enforcing one of the special structures described in Section III. More specifically, the minimizer of (11) with respect to  $\mathbf{C}_p \in \mathcal{P}_i^S \cap \mathcal{H}_N^{++}$  can be found as the optimal solution to the following constrained minimization problem:

$$\begin{cases} \min_{\mathbf{C}_p} & \log |\mathbf{C}_p| + \text{tr} \{ \hat{\mathbf{C}}_p \mathbf{C}_p^{-1} \} \\ \text{s.t.} & \mathbf{C}_p \in \mathcal{P}_i^S \cap \mathcal{H}_N^{++}, i = 1, \dots, 4 \end{cases} \quad (12)$$

where

$$\hat{\mathbf{C}}_p(\mathbf{C}_t) = \frac{1}{M} \sum_{k=1}^M \sum_{l=1}^M \hat{\mathbf{S}}^{kl} \mathbf{C}_t^{-1}(l, k), \quad (13)$$

with  $\hat{\mathbf{S}}^{kl}$  the  $(k, l)$ -th block of size  $N \times N$  in the matrix  $\hat{\mathbf{S}}$ , and  $\mathbf{C}_t^{-1}(l, k)$  the  $(k, l)$ -th element of the matrix  $\mathbf{C}_t^{-1}$ . Note that Problem (12) is formally analogous to the problem presented in [24, eq. 11], with  $\hat{\mathbf{C}}_p$  replacing the SCM. Consequently, the principal technical result of [24] can be applied to derive the ML estimation of the structured polarimetric covariance matrix  $\mathbf{C}_p$ . Thus, the optimal solution  $\mathbf{C}_p$  is provided below for each

specified structural constraint, using the matrix statistic  $\hat{\mathbf{C}}_p$  as starting point.

1) No symmetry:

$$\check{\mathbf{C}}_p = \hat{\mathbf{C}}_p. \quad (14)$$

2) Reflection symmetry:

$$\check{\mathbf{C}}_p = \mathbf{U}^H \begin{bmatrix} \tilde{\mathbf{S}}_{1,1} & \mathbf{0} \\ \mathbf{0} & \tilde{\mathbf{S}}_{3,3} \end{bmatrix} \mathbf{U} \quad (15)$$

where  $\tilde{\mathbf{S}} = \mathbf{U} \hat{\mathbf{C}}_p \mathbf{U}^H = \begin{bmatrix} \tilde{\mathbf{S}}_{1,1} & \tilde{\mathbf{S}}_{1,3} \\ \tilde{\mathbf{S}}_{3,1} & \tilde{\mathbf{S}}_{3,3} \end{bmatrix}$ , and

$$\mathbf{U} = \begin{bmatrix} 1 & 0 & 0 \\ 0 & 0 & 1 \\ 0 & 1 & 0 \end{bmatrix}.$$

3) Rotation symmetry:

$$\check{\mathbf{C}}_p = \mathbf{T}^H \mathbf{E}^{-1} \mathbf{V}^H \begin{bmatrix} \tilde{\mathbf{S}}_{1,1} & \mathbf{0} \\ \mathbf{0} & \frac{1}{2} (\tilde{\mathbf{S}}_{2,2} + \mathbf{J} \tilde{\mathbf{S}}_{2,2} \mathbf{J}) \end{bmatrix} \mathbf{V} \mathbf{E}^{-1} \mathbf{T} \quad (16)$$

where  $\tilde{\mathbf{S}} = \mathbf{V} \mathbf{E} \mathbf{T} \hat{\mathbf{C}}_p \mathbf{T}^H \mathbf{E}^H \mathbf{V}^H = \begin{bmatrix} \tilde{\mathbf{S}}_{1,1} & \tilde{\mathbf{S}}_{1,2} \\ \tilde{\mathbf{S}}_{2,1} & \tilde{\mathbf{S}}_{2,2} \end{bmatrix}$ , and

$$\mathbf{E} = \begin{bmatrix} 1 & 0 & 0 \\ 0 & 1/\sqrt{2} & 0 \\ 0 & 0 & 1 \end{bmatrix}, \quad \mathbf{T} = \frac{1}{\sqrt{2}} \begin{bmatrix} 1 & 0 & 1 \\ 1 & 0 & -1 \\ 0 & \sqrt{2} & 0 \end{bmatrix},$$

$$\mathbf{V} = \begin{bmatrix} 1 & 0 & 0 \\ 0 & 0 & j \\ 0 & 1 & 0 \end{bmatrix}.$$

4) Azimuth symmetry:

$$\check{\mathbf{C}}_p = \mathbf{T}^H \mathbf{E}^{-1} \mathbf{diag} \left( \tilde{\mathbf{S}}_{1,1}, \frac{\tilde{\mathbf{S}}_{2,2} + \tilde{\mathbf{S}}_{3,3}}{2}, \frac{\tilde{\mathbf{S}}_{2,2} + \tilde{\mathbf{S}}_{3,3}}{2} \right) \mathbf{E}^{-1} \mathbf{T} \quad (17)$$

where  $\tilde{\mathbf{S}} = \mathbf{E} \mathbf{T} \hat{\mathbf{C}}_p \mathbf{T}^H \mathbf{E}$  and  $\tilde{\mathbf{S}}_{1,1}$ ,  $\tilde{\mathbf{S}}_{2,2}$ ,  $\tilde{\mathbf{S}}_{3,3}$  are its diagonal entries.

**Optimization over  $\mathbf{C}_t$ .** As in the previous case, for a fixed  $\mathbf{C}_p$ , the minimizer of (11) with respect to  $\mathbf{C}_t \in \mathcal{H}_M^{++}$  can be found as the optimal solution to the following minimization problem:

$$\begin{cases} \min_{\mathbf{C}_t} & \log |\mathbf{C}_t| + \text{tr} \{ \hat{\mathbf{C}}_t \mathbf{C}_t^{-1} \} \\ \text{s.t.} & \mathbf{C}_t \in \mathcal{H}_M^{++} \end{cases} \quad (18)$$

whose optimal solution is given by

$$\hat{\mathbf{C}}_t(\mathbf{C}_p) = \frac{1}{N} \sum_{k=1}^N \sum_{l=1}^N \bar{\mathbf{S}}^{kl} \mathbf{C}_p^{-1}(l, k) \quad (19)$$

where

$$\bar{\mathbf{S}} = \mathbf{K}_{M,N}^T \hat{\mathbf{S}} \mathbf{K}_{M,N} \quad (20)$$

and  $\bar{\mathbf{S}}^{kl}$  is the  $(k, l)$ -th block of  $M \times M$  in the matrix  $\bar{\mathbf{S}}$ . The permutation matrix  $\mathbf{K}_{M,N}$  is defined such that

$$\mathbf{K}_{M,N} \text{vec}\{\mathbf{A}\} = \text{vec}\{\mathbf{A}^T\}, \quad (21)$$

for any  $M \times N$  matrix  $\mathbf{A}$ , and its explicit form is given by

$$\mathbf{K}_{M,N} = \sum_{i=1}^M \sum_{j=1}^N (E_{ij} \otimes E_{ji}), \quad (22)$$

where  $E_{ij}$  is an  $M \times N$  matrix with 1 in the  $(i, j)$ -th position and 0 elsewhere. For instance, for  $N = 3$  and  $M = 2$ , it is

$$\mathbf{K}_{2,3} = \begin{pmatrix} 1 & 0 & 0 & 0 & 0 & 0 \\ 0 & 0 & 1 & 0 & 0 & 0 \\ 0 & 0 & 0 & 0 & 1 & 0 \\ 0 & 1 & 0 & 0 & 0 & 0 \\ 0 & 0 & 0 & 1 & 0 & 0 \\ 0 & 0 & 0 & 0 & 0 & 1 \end{pmatrix} \quad (23)$$

Note that, since  $\hat{\mathbf{S}}$  is a psd matrix, also,  $\hat{\mathbf{C}}_p$  in (13) and  $\hat{\mathbf{C}}_t$  in (19) are psd matrices [36].

To solve the problem in (10), the flip-flop which involves alternating minimization with respect to  $\mathbf{C}_t$  and  $\mathbf{C}_p$  (keeping one of them fixed at a time) is hence applied. Its main steps are reported in Algorithm 1.

---

**Algorithm 1** Flip-flop algorithm with polarimetric symmetry structure

---

**Input:**  $K, \mathbf{X}$  (constructed as described in Section III).

**Output:**  $\hat{\mathbf{C}}_p, \hat{\mathbf{C}}_t$  for each symmetry.

- 1: Initialize  $\hat{\mathbf{C}}_t = \mathbf{C}_t^{init}$  by an arbitrary psd matrix.
  - 2: Calculate  $\hat{\mathbf{C}}_p$  using (13) with the previous  $\hat{\mathbf{C}}_t$ .
  - 3: Force the symmetry structure, by calculating the ML estimate  $\check{\mathbf{C}}_p$  as in (14), (15), (16) or (17) using  $\hat{\mathbf{C}}_p$  as starting point.
  - 4: Set  $\hat{\mathbf{C}}_p = \check{\mathbf{C}}_p$ .
  - 5: Calculate the new value of  $\hat{\mathbf{C}}_t$  using (19), with the updated  $\hat{\mathbf{C}}_p$  in the previous step.
  - 6: Iterate steps 2-5 until convergence.
- 

**Remark 1.** It is worth noting that, the proposed flip-flop estimation procedure (assuming the existence of the ML estimate) exhibits the following feature properties [42], [43]:

- the sequence of produced negative log-likelihood values is bounded below;
- the sequence of produced negative log-likelihood values is monotonically decreasing and converges to a finite value. Moreover, for any cluster point, the corresponding negative log-likelihood value attains this limit value;
- any cluster point of the produced sequence of estimates is a stationary solution to Problem (11) and the corresponding negative log-likelihood value attains this aforementioned limit value.

## V. CLASSIFICATION OF DOMINANT SYMMETRY BY MODEL ORDER SELECTION

The framework outlined in this section identifies the pre-dominant special structure of the polarimetric covariance matrix characterizing the scattering mechanism of a given pixel.

This allows the problem to be treated as a data classification task based on the scattering properties of the target pixel and its neighboring pixels. As a result, the classification problem is formulated as a multiple hypothesis test that includes both nested and non-nested hypotheses, that is:

$$\begin{cases} H_1 : & \text{no symmetry;} \\ H_2 : & \text{reflection symmetry;} \\ H_3 : & \text{rotation symmetry;} \\ H_4 : & \text{azimuth symmetry.} \end{cases} \quad (24)$$

The decision is taken resorting to MOS criteria [26], [27], selecting the hypothesis  $H_{i^*}$  according to

$$i^* = \arg \min_{i=1,\dots,4} \left[ 2l(\hat{\mathbf{C}}_{(i)}; \mathbf{X}) + \zeta \eta(K) \right], \quad (25)$$

where  $\hat{\mathbf{C}}_{(i)}$  is the ML estimate of  $\mathbf{C}$  under the  $H_i$  hypothesis comprising  $\zeta = \zeta_t + \zeta_p$  parameters, with  $\zeta_t = M^2$ , whereas  $\zeta_p$  are as detailed in Section III. The quantity  $\zeta \eta(K)$  represents the penalty coefficient used to prevent overfitting [27]. Indeed, as the negative log-likelihood in (25) decreases with increasing  $\zeta$  (for nested models), the second term correspondingly increases. Moreover, different selection strategies diversify due to the definition of the penalty, namely:

- AIC (Akaike information criterion):  $\eta(K) = 2$ ;
- GIC (generalized information criterion):  $\eta(K) = \delta + 1$ , with  $\delta$  an integer number greater than or equal to 2;
- BIC (Bayesian information criterion):  $\eta(K) = \log(K)$ ;
- HQC (Hannan-Quinn information criterion) [44]:  $\eta(K) = 2 \log(\log(K))$ .

Finally, taking into account the statistical hypotheses regarding the data, i.e., by substituting the expression of  $l(\hat{\mathbf{C}}_{(i)}; \mathbf{X})$  in (25), the synthesized MOS rules become

$$i^* = \arg \min_{i=1,\dots,4} \left[ 2K \log |\hat{\mathbf{C}}_{(i)}| + 2K \text{tr}(\hat{\mathbf{C}}_{(i)}^{-1} \hat{\mathbf{S}}) + \zeta \eta(K) \right] \quad (26)$$

A summary of the generic classification scheme is illustrated in Algorithm 2.

---

**Algorithm 2** MOS algorithm for symmetry classification

---

**Input:**  $\hat{\mathbf{C}}_t, \hat{\mathbf{C}}_p$  for each specific symmetry (constructed as described in Section IV).

**Output:**  $H_{i^*}$ , i.e., the selected dominant symmetry.

- 1: Calculate the decision statistic with (26) using the founded  $\hat{\mathbf{C}}_t$  and  $\check{\mathbf{C}}_p$  for each symmetry, and a specific MOS criterion, viz., AIC, GIC, BIC or HQC.
  - 2: Select the hypothesis (resp. symmetry) which corresponds to the minimum decision statistic.
- 

## VI. PERFORMANCE ANALYSIS AND DISCUSSIONS

This section is intended to evaluate the effectiveness of the proposed polarimetric covariance symmetry classification framework for multitemporal PolSAR images. To this end, both quantitative analyses on simulated data and assessments on measured PolSAR data are performed.

### A. Quantitative analysis on simulated data

This subsection evaluates the performance of the proposed covariance symmetry classification scheme for multitemporal PolSAR images. The first analysis is conducted to quantify the accuracy of the proposed flip-flip in estimating the polarimetric covariance matrix. Hence, the normalized root mean square error (RMSE) is used as performance metric, which is defined as

$$\text{NRMSE} = \sqrt{\mathbb{E} \left[ \frac{\|C_p - \check{C}_p\|^2}{\|C_p\|^2} \right]}. \quad (27)$$

Noteworthy, due to the lack of a closed-form expression for the normalized RMSE in (27), the statistical expectation is approximated resorting to the classic Monte Carlo approach, that is

$$\text{NRMSE} = \sqrt{\frac{1}{M_c} \sum_{m=1}^{M_c} \frac{\|C_p - \check{C}_p^{(m)}\|^2}{\|C\|^2}}, \quad (28)$$

where  $\check{C}_p^{(m)}$  is the estimate of  $C_p$  obtained at the  $m$ -th Monte Carlo run and  $M_c$  is the number of trials. Moreover, as a term of comparison, the structured ML covariance estimator assuming independent and identically distributed polarimetric data in different temporal looks, i.e., supposing the absence of temporal correlation, is considered. Precisely, the structured ML covariance estimate is obtained applying the classification procedure of [24], where the SCM is replaced by the average of the two SCMs obtained from two distinct data subsets, each of size  $K$ . Hence, it is denoted as temporal uncorrelated structured ML (TUSML) for short in the next analyses.

Differently, the second analysis concentrates on assessing the effectiveness of the MOS rules devised in Section V in terms of its capabilities to correctly detect (or classify) the true symmetry. To this end, the accuracy (which also represents the probability of correctly selecting a specific structure) as well as the confusion matrix are introduced as a performance metric. Due to the lack of a closed-form expression for the accuracy, it is computed resorting to the classic Monte Carlo approach as the ratio between the number of times a specific symmetry is selected over the total number of trials,  $M_c$ , set equal to  $10^4$ .

The considered simulation scenario consists of  $K$  zero-mean complex circular Gaussian vectors of size  $3M$ , which are colored with a specific nominal covariance. Specifically, the nominal covariance matrix for each of the considered four scenarios (no symmetry, reflection, rotation, and azimuth symmetry) is  $C_i = C_t \otimes C_{p_i}$ ,  $i = 1, \dots, 4$ . Regarding the temporal covariance matrix, two different situations are studied, i.e.,  $C_t = I$  (uncorrelated data), and  $C_t(n, m) = \rho^{|n-m|}$ ,  $\{n, m\} = 1, \dots, M$ ,  $|\rho| < 1$  (correlated data with exponentially shaped covariance structure). Differently, the nominal polarimetric covariances for the four scenarios are defined, respectively, as [24]

$$C_{p_1} = \begin{bmatrix} 1 & 0.2 + 0.3j & 0.5 - 0.3j \\ 0.2 - 0.3j & 0.25 & -0.2 - 0.2j \\ 0.5 + 0.3j & -0.2 + 0.2j & 0.8 \end{bmatrix}, \quad (29)$$

$$C_{p_2} = \begin{bmatrix} 1 & 0 & 0.5 - 0.3j \\ 0 & 0.25 & 0 \\ 0.5 + 0.3j & 0 & 0.4 \end{bmatrix}, \quad (30)$$

$$C_{p_3} = \begin{bmatrix} 1 & 0.3j & 0.2 \\ -0.3j & 0.4 & 0.3j \\ 0.2 & -0.3j & 1 \end{bmatrix}, \quad (31)$$

$$C_{p_4} = \begin{bmatrix} 1 & 0 & 0.5 \\ 0 & 0.25 & 0 \\ 0.5 & 0 & 1 \end{bmatrix}. \quad (32)$$

All the analyses are conducted with the flip-flop algorithm initiated with the identity matrix for  $\hat{C}_t$  and executed with 5 iterations. This number is chosen since the negative log-likelihood in (11) does not undergo significant variations beyond this amount of steps. As an example, the readers may refer to Figure 2 for the above simulation scenario with  $M = 2$  and  $K = 6$ .

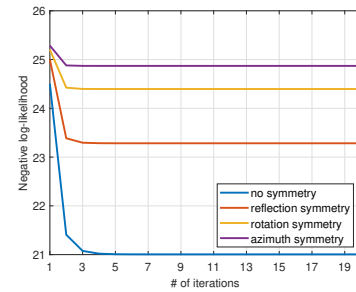


Figure 2: Negative log-likelihood (evaluated over  $M_c = 10^4$  Monte Carlo trials) versus the number of iterations in the flip-flop algorithm for  $M = 2$  simulated data with exponentially shaped  $C_t$  with  $\rho = 0.9$ , and  $K = 6$ .

**Normalized RMSE analysis.** The normalized RMSE is shown versus the number of samples in Figure 3 for the proposed flip-flop and the TUSML. The simulated scenario assumes  $C_t = I$ , namely temporal uncorrelation, and  $M = 2$ , i.e., two temporal acquisitions, where subplots refer to different structures for  $C_p$  (both in terms of data generation and adopted structured ML estimate). Similarly, Figure 4 shows the normalized RMSE versus the number of samples for the same simulation setting, except for the introduction of temporal correlation, i.e.,  $C_t$  is exponentially shaped with  $\rho = 0.9$ . Interestingly, for the scenario of Figure 3 assuming temporal independence, the TUSML slightly overcomes the proposed flip-flop in the presence of a reduced number of spatial samples, for all the considered structures. While, in all the other circumstances, namely in the presence of correlation between the data, the proposed flip-flop demonstrates its superiority. The observed behaviors can be explained by noting that, in the first case, the algorithm requires more data to achieve the same performance due to the high number of unknowns. In

contrast, in the second case, while the TUSML experiences a model mismatch, the flip-flop method does not. Moreover, as expected, both the estimators under all the considered scenarios improve their performance as the number of looks increases.

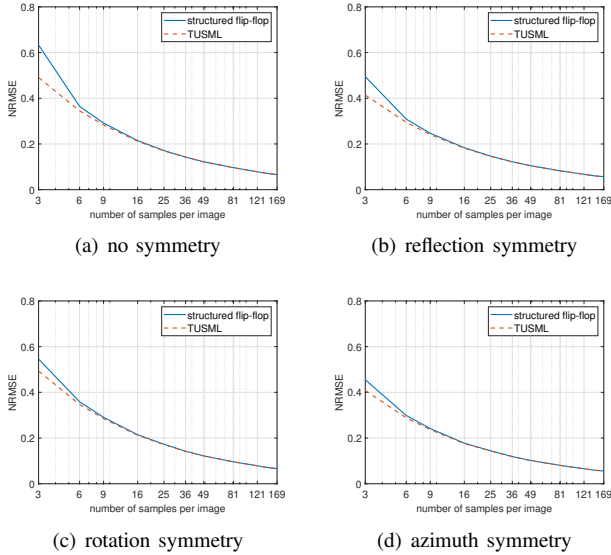


Figure 3: Normalized RMSE (evaluated over  $M_c = 10^4$  Monte Carlo trials) of the polarimetric covariance estimate versus the number of samples per subset. The curves refer to the proposed flip-flop and the TUSML. Data are simulated according to the described Gaussian model setting  $M = 2$  and  $C_t = \mathbf{I}$ . Subplots refer to the nominal  $C_p$  having a) no symmetry, b) reflection symmetry, c) rotation symmetry, and d) azimuth symmetry.

**Classification capabilities analysis.** To further shed light on the capabilities of the proposed framework of correctly selecting the proper polarimetric covariance structure, an analysis in terms of accuracy is herein reported and discussed. In Figure 5, the confusion matrix (expressed in percentage) is shown for data generated according to the above described Gaussian model for each one of the polarimetric structures in (29)-(32), assuming  $K = 25$  looks, and  $M = 2$  temporal instances. Hence, each subplot in the figure refers to each of the MOS rules described in Section V, viz., AIC, BIC, GIC (with  $\delta = 2$ ), and HQC. Moreover, the four classes are representative of the nominal polarimetric structure. Therefore, for each hypothesis (i.e., each nominal symmetry), the probability of selecting each possible structure is described by each row in the confusion matrix.

From the inspection of these results, it is evident that all the considered MOS rules are in general capable of identifying the nominal structure in the polarimetric covariance. It also turns out that azimuth symmetry is the most difficult to identify, as it can be seen as a special case of all the other structures, as shown by the lowest accuracy values, for each considered MOS. Nevertheless, both the BIC and GIC demonstrate to be the most effective classification rules, outperforming both the AIC and HQC counterparts. Moreover, they ensure an

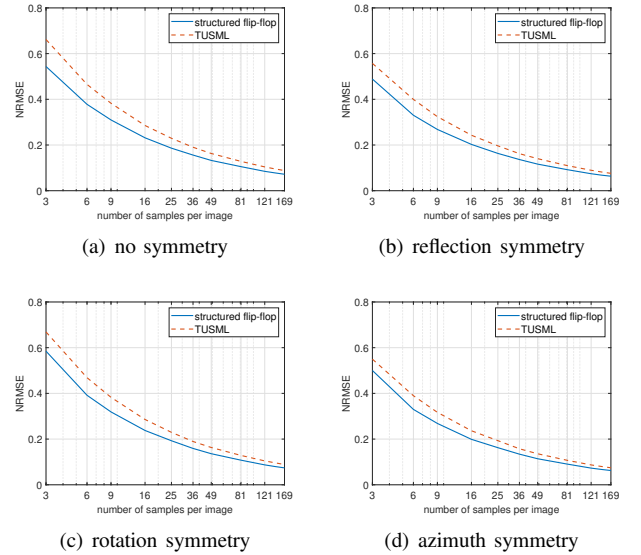


Figure 4: Normalized RMSE (evaluated over  $M_c = 10^4$  Monte Carlo trials) of the polarimetric covariance estimate versus the number of samples per subset. The curves refer to the proposed flip-flop and the TUSML. Data are simulated according to the described Gaussian model setting  $M = 2$  and exponentially shaped  $C_t$  with  $\rho = 0.9$ . Subplots refer to the nominal  $C_p$  having a) no symmetry, b) reflection symmetry, c) rotation symmetry, and d) azimuth symmetry.

accuracy greater than the 90% also for the challenging azimuth symmetry case. Interestingly, the BIC allows reaching the best performance without the necessity of setting any tuning parameter.

To grasp more information on the behavior of the considered selectors, in Figure 6 the confusion matrices are also shown for the same simulation setting as above, but for a larger number of looks, i.e.,  $K = 49$ . In this case, also the HQC exceed the 90% threshold value in the detection of the first three structures, approaching this value even in the case of azimuth symmetry. However, it is evident that there is a growth in the performance for all the detection rules regardless of the assumed polarimetric structure. This fact can be explained observing that increasing the number of looks  $K$  leads to a more and more accurate estimate of the sample covariance matrix that is at the base of all the estimates obtained from the proposed flip-flop.

Finally, to directly compare the various adopted MOS rules, we present in Table I the values of Cohen's kappa coefficient [45],  $\kappa$ , for the same simulation setups as in Figures 5 and 6. Interestingly, the values of  $\kappa$  confirm the trends discussed above. Specifically, an increased number of looks leads to a higher coefficient value for all the proposed selectors. Furthermore, the BIC is confirmed to be the best, achieving a Cohen's kappa coefficient close to 1 in both cases for  $K = 25$  and  $K = 49$ .

To further corroborate the previous results, in Table II the accuracy of each class (i.e., each nominal covariance) is summarized with reference to the BIC rule, having it

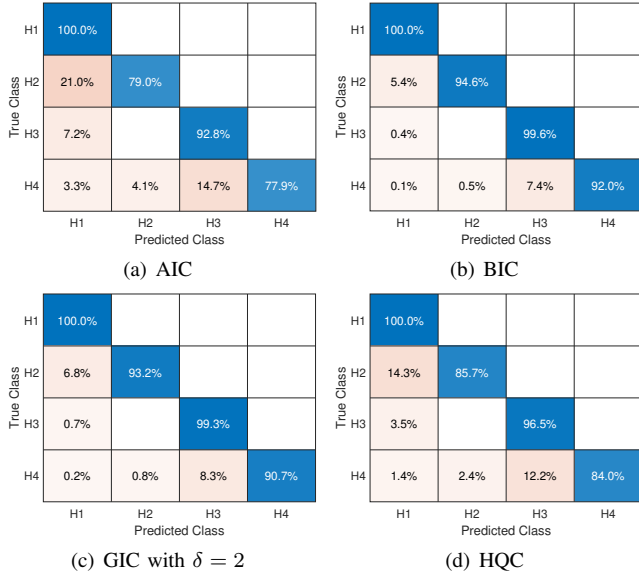


Figure 5: Confusion matrix for the considered MOS rules (for the classes of no symmetry, reflection symmetry, rotation symmetry, and azimuth symmetry), using  $K = 25$  looks with  $M = 2$  and  $C_t = I$ . Subplots refer to the MOS rules a) AIC, b) BIC, c) GIC, and d) HQC.

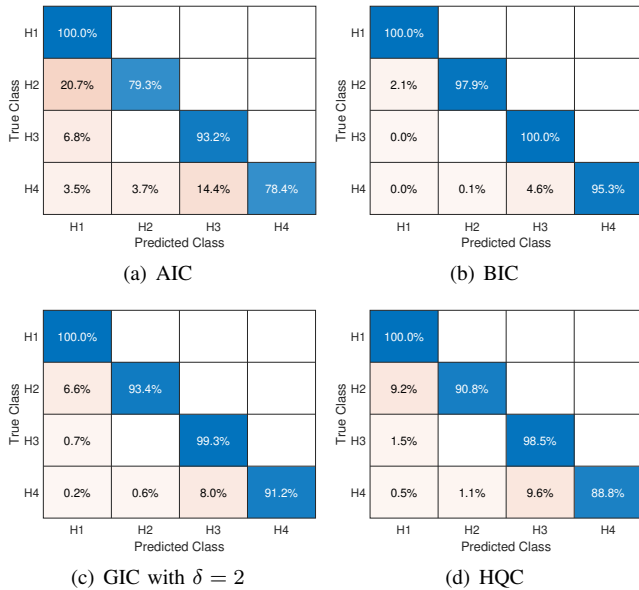


Figure 6: Confusion matrix for the considered MOS rules (for the classes of no symmetry, reflection symmetry, rotation symmetry, and azimuth symmetry), using  $K = 49$  looks with  $M = 2$  and  $C_t = I$ . Subplots refer to the MOS rules a) AIC, b) BIC, c) GIC, and d) HQC.

shown the best performance in the confusion matrices of Figures 5-6. Specifically, the reported values correspond to different number of looks, viz.,  $K = (6, 9, 25)$ , as well as to an exponentially shaped temporal covariance  $C_t$  with correlation coefficient  $\rho = 0.9$ , whose size  $M$  varies from 2 to 4. Additionally, for comparison, the results of the classifier designed in [24] for a single datum (i.e.,  $M = 1$ ) are provided

Table I: Cohen's kappa coefficient,  $\kappa$ , for the considered MOS rules for the simulation setups of Figures 5 and 6.

	AIC	BIC	GIC	HQC
$K = 25$	0.83	0.95	0.94	0.89
$K = 49$	0.84	0.98	0.95	0.93

to complete the analysis. In agreement with the previous results, the values in the table demonstrate the BIC increasing ability to accurately detect the correct symmetry as the number of available data points grows. For example, with regard to azimuth symmetry and considering  $M = 2$ , it is observed that the accuracy significantly increases from 70.8% when  $K = 6$  to 92.0% when  $K = 25$ . Analogously, the impact of the number of temporal instances can be also observed analyzing the accuracy as  $M$  varies. As an example, with reference to the average accuracy over all symmetries and  $K = 6$ , it can be seen that it increases of an amount more than 6% considering  $M = 4$  in place of  $M = 1$ . These improved classification results suggest that the overall system performance can be enhanced when a stack of temporal data is used. Finally, it is important to note that the performance is not highly sensitive to temporal correlation (results for different  $\rho$  values are omitted for brevity). This, however, can be intuitively explained, as the symmetry is related to the polarimetric part of the covariance matrix, and the Kronecker structure enables the separation of the temporal and spatial contributions.

Finally, to complete this quantitative analysis on simulated data, the proposed method using the BIC rule is compared with the corresponding TUSML for the previously described simulation scenario, employing  $K = 25$  looks and an exponentially shaped temporal covariance  $C_t$  with a correlation coefficient of  $\rho = 0.9$  and size  $M = 2$ . The results are still presented in terms of confusion matrices in Figure 7. A direct comparison of the two matrices clearly shows that, based on the results illustrated above, the proposed framework improves the classification performance compared to the competitor, which does not account for temporal correlation. Focusing on specific values, it is interesting to note that the new method significantly increases the accuracy for the reflection symmetry case with respect to the TUSML, i.e., from 72.5% to 94.6%. Analogously, the azimuth symmetry accuracy increases from 72.6% to 92.0%. Finally, a comparison of the Cohen's kappa coefficients further quantifies this behavior. In fact, the value achieved by the proposed method is  $\kappa = 0.95$ , which significantly exceeds that of TUSML, where  $\kappa = 0.78$ .

## B. Assessment on measured data

The focus of this section is to evaluate the effectiveness of the proposed covariance symmetry classification scheme for multi-temporal PolSAR images. To do this, some experiments on real-recorded PolSAR datasets are conducted, concentrating on the use of the BIC selector, since it has shown the best performance on simulated data. Moreover, as for the analyses on simulated data, the proposed flip-flop is run for five iterations and with the estimate of  $C_t$  initialized to the identity matrix.

Table II: Accuracy (%) using the BIC selection rule for an exponentially shaped  $C_t$ , with  $\rho = 0.9$ .

	$K = 6$				$K = 9$				$K = 25$			
	$M = 1$	$M = 2$	$M = 3$	$M = 4$	$M = 1$	$M = 2$	$M = 3$	$M = 4$	$M = 1$	$M = 2$	$M = 3$	$M = 4$
<b>No Symmetry</b>	99.9%	100%	100%	100%	100%	100%	100%	100%	100%	100%	100%	100%
<b>Reflection symmetry</b>	73.4%	68.4%	70.0%	72.1%	88.2%	80.2%	81.23%	83.0%	98.5%	94.6%	94.8%	94.9%
<b>Rotation symmetry</b>	75.2%	85.2%	87.6%	88.0%	91.1%	94.1%	94.9%	95.6%	99.5%	99.6%	99.6%	99.6%
<b>Azimuth symmetry</b>	58.4%	70.8%	71.7%	72.6%	74.7%	81.0%	81.4%	81.8%	90.6%	92.0%	92.6%	92.6%
<b>Average accuracy</b>	76.7%	81.1%	82.3%	82.9%	88.5%	88.8%	89.4%	90.1%	97.1%	96.6%	96.7%	96.8%

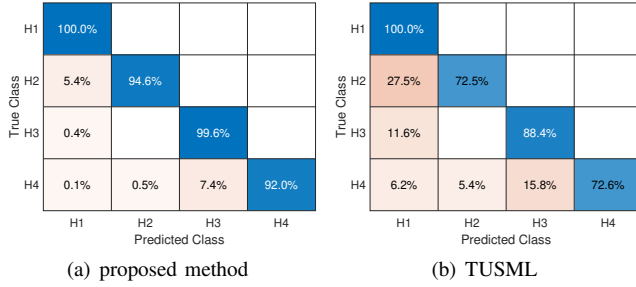


Figure 7: Confusion matrix for the BIC selection rule (for the classes of no symmetry, reflection symmetry, rotation symmetry, and azimuth symmetry), using  $K = 25$  looks with  $M = 2$  and an exponentially shaped  $C_t$ , with  $\rho = 0.9$ . Subplots refer to a) the proposed structured flip-flop based method, and b) TUSML.

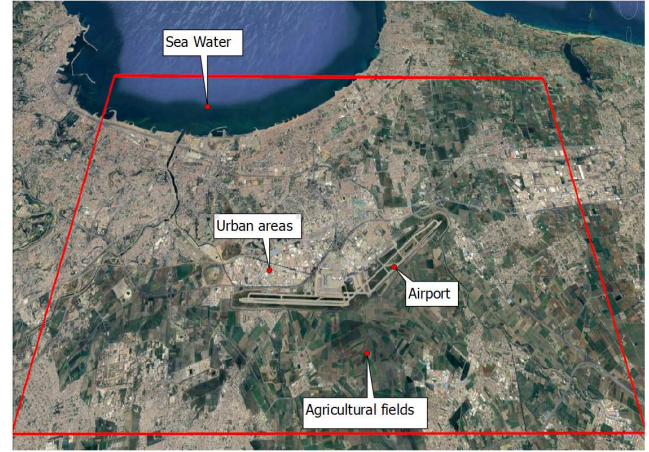


Figure 8: Google Earth© image with a polygon outlining the studied area.

The study is conducted using data collected over an area of Algeria, encompassing regions with diverse surface features and various land uses. This includes a portion of the Mediterranean Sea, coastline, an international airport, urban areas, and agricultural fields. The utilized PolSAR data comprise two fully polarized RADARSAT-2 images, acquired on two different dates with an interval of 24 days (i.e., April 11th, 2009, and May 5th, 2009), with the same incidence angles. For our analysis, the selected area of interest is a sub-image of  $1750 \times 2500$  pixels (i.e.,  $L = 1750$  and  $C = 2500$ ). A picture representing the optic image extracted from Google Earth©, with a polygon delimiting the area of interest, is drawn in Figure 8. Finally, the sensor parameters are reported in Table III.

Table III: RADARSAT-2 parameters.

Parameter	Quantity
Wavelength	5.5 [cm]
Sensor altitude	798 [km]
Incidence angle	38.34 to 39.81 [degrees]
Nominal resolution [range $\times$ azimuth]	$5.2 \times 7.6$ [m]
Sampled pixel & line spacing	$4.73 \times 4.74$ [m]
Look direction	right
Pass	descending
Acquisition mode	fine quad polarization

In Figure 9, with reference to the RADARSAT-2 images, the symmetries classified through the proposed framework with the BIC rule are plotted. More precisely, the estimations are done using a sliding window of size  $5 \times 5$ , hence with  $K = 25$ . The two subplots refer to a) the method developed in [24] for a single image, and b) the proposed algorithm. Moreover, for each pixel of the considered scene, a specific color is used

for each hypothesis selected by the test, viz. no symmetry (black), reflection symmetry (blue), rotation symmetry (red), and azimuth symmetry (yellow).

From a first visual inspection of the colored maps, it is evident that the seawater is, as expected, mostly detected as reflection symmetry. Moreover, pixels belonging to the airport runway are also classified as having a reflection symmetry structure. This is not surprising, observing that the runway has a plane structure [23], [25]. Similarly, also the uncultivated agricultural areas under the airport are classified as being structured with a reflection symmetry. Going further into the details, it can be also ascertained that the vegetation is revealed to be azimuthal symmetry, whereas building are essentially related to absence of symmetry. Finally, the rotation symmetry is detected few times in the entire image, therefore not giving significant information for this specific environment. Now, comparing the results obtained from the algorithm working on the single image with the proposed one exploiting the information embedded in the pair, interesting conjectures can be done. Initially, the most noticeable difference is that areas with some vegetation are much more distinct. The proposed method has classified these areas as having azimuthal symmetry (which aligns with this specific class), whereas the standard method identifies them as having reflection symmetry. Furthermore, in the proposed map, the separation between homogeneous areas appears to be much more evident with sharper boundaries than the counterpart. As a matter of fact, the runway in the proposed case is much better visible than in the single image processing.

Similarly, the coastline appears sharper and better detected. Finally, also building in the image (see the black areas) are

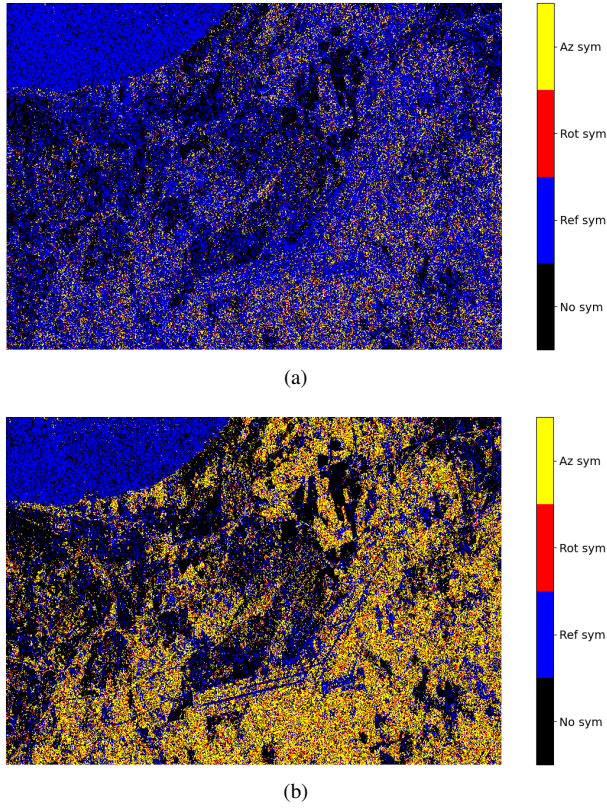


Figure 9: Symmetries classification using BIC with  $K = 25$ . Subplots refer to a) algorithm of [24] for single image, b) proposed method with  $M = 2$ .

better emphasized. These effects are also related to the fact that, using both images as in the proposed methodology, the resulting map appears less noisy with homogeneous areas displayed cleaner. Indeed, using a multi-temporal dataset for the same value of  $K$  produces a better classification map than relying on a single image.

**Zone index  $H/\bar{\alpha}$  decomposition.** Once the polarimetric covariance symmetries have been classified, for each pixel an estimate of the covariance with the detected structure is hence available. Accordingly, a more detailed analysis of their effect on the interpretation of the scene can be performed. Specifically, the classic  $H/\bar{\alpha}$  classification [6] is compared with an enhanced version that employs a more accurate estimate, namely, the structured covariance estimates provided by the proposed flip-flop algorithm, instead of the SCM<sup>2</sup>. Hence, once the images have been decomposed into the  $H/\bar{\alpha}$ , different areas are classified by means of the zone index as proposed in [6], as specified in the following:

<sup>2</sup>The structured covariance used in this paper is associated with a polarimetric vector organized as  $\mathbf{y} = [y_{HH}, y_{HV}, y_{VV}]^T$ . Differently, to perform the  $H/\bar{\alpha}$  classification, the starting point is the coherence obtained using the Pauli vector [7],  $\mathbf{y}_P = (1/\sqrt{2})[(y_{HH} + y_{VV}), (y_{HH} - y_{VV}), 2y_{HV}]^T$ . For the above reasons, the following transformation must be applied to  $\hat{\mathbf{C}}_p$  in order to derive the proper coherence  $T_P = T\hat{\mathbf{G}}\hat{\mathbf{C}}_p\hat{\mathbf{G}}^T$ , with

$$\hat{\mathbf{G}} = \begin{bmatrix} 1 & 0 & 0 \\ 0 & \sqrt{2} & 0 \\ 0 & 0 & 1 \end{bmatrix}.$$

- Class  $Z_1$ : Double bounce scattering in a high entropy environment;
- Class  $Z_2$ : Multiple scattering in a high entropy environment (e.g. forest canopy);
- Class  $Z_3$ : Surface scattering in a high entropy environment;
- Class  $Z_4$ : Medium entropy multiple scattering;
- Class  $Z_5$ : Medium entropy vegetation (dipole) scattering;
- Class  $Z_6$ : Medium entropy surface scattering;
- Class  $Z_7$ : Low entropy multiple scattering (double or even bounce scattering);
- Class  $Z_8$ : Low entropy dipole scattering (strongly correlated mechanisms with a large imbalance in amplitude between HH and VV);
- Class  $Z_9$ : Low entropy surface scattering (e.g. Bragg scatter and rough surfaces).

This is reported in Figure 10, where the zone indexes relative to the  $H/\bar{\alpha}$  plane are shown with reference to the classic sample coherence in subplot a) and the proposed structured covariances in subplot b).

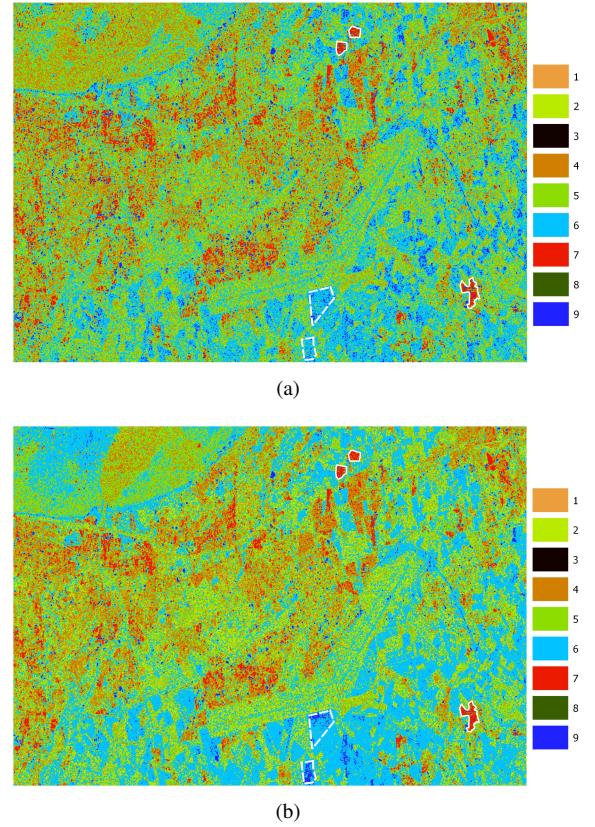


Figure 10: Zone index  $H/\bar{\alpha}$  decomposition of the RADARSAT-2 data using  $K = 25$  looks. Subplots refer to a) sample coherence matrix, b) reconstructed matrix with the proposed method based on flip-flop.

Comparing the two zone index maps, it can be observed that the proposed framework improves the classification of buildings as *dihedrals* (class 7), with some unseeded lands being classified as *surface* (class 9) instead of *anisotropic particles* (class 5). Furthermore, marine pollution (see e.g.

[46]) is well illustrated, while it is completely missed in the classic approach. To better quantify these results, two areas of coverage are selected based on the homogeneity and predictability of classes, namely urban areas, and agricultural lands. These are indicated in Figure 10, where dense urban areas refer to the three patches delineated by solid lines, whereas the agricultural lands are indicated with the dashed lines. For each environment mentioned above, the percentage of pixels belonging to the classes detected according to the  $H/\bar{\alpha}$  plane is reported in Table IV. To go into detail, it can be seen that for urban areas, the percentage of pixels associated with the class 7 describing multiple scattering (as expected for this environment) increases from 60.01% with the classic (sample covariance based)  $H/\bar{\alpha}$  plane to 68.2% with the proposed approach. Regarding agricultural land zones, instead, it is clearly observed that the proposed method increases the percentage of pixels classified as  $Z_9$  (i.e., surface), from 13.56% with the classic method to 26.52%. This is not surprising, since a lower entropy indicates more homogeneous targets, as expected for the agricultural fields. Finally, being class  $Z_3$  a *nonfeasible region* in the  $H/\bar{\alpha}$  plane [7], it is considered a number as small as possible of entries classified as belonging to this class (ideally empty). However, in some cases for the agricultural lands, a few pixels could be misclassified as  $Z_3$  due to factors such as numerical errors or convergence issues related to the decomposition process. Interestingly, the proposed approach allows reducing this percentage from 0.28% of the standard method to 0.13%.

**Freeman-Durden Wishart classification.** The last analysis consists in performing the Freeman-Durden Wishart classification as proposed in [19] to further show the impact of a more accurate covariance estimate in emphasizing details within the image. This method categorizes the data into three main types based on the dominant scattering mechanisms:

- 1) surface scattering,
- 2) volume scattering,
- 3) double bounce.

The above categories are further subdivided into 16 subclasses [19]. Moreover, a fourth category is also designated for mixed scattering pixels that do not clearly fit into any of the three primary scattering mechanisms (it is denoted as *no dominant*). The results of the classification process are illustrated in Figure 11, while the subclasses grouped according to the dominant mechanism are presented in Figure 12. The procedure is done again using the estimated  $C_p$  relying on the proposed BIC selection rule, in comparison with the classic Freeman-Durden Wishart classification initialized by the sample coherence.

To quantify the results, the analysis of the classification process based on the two coherence estimates are conducted over three distinct zones. The zones, highlighted in Figure 11 and labelled as *Field 1*, *Field 2*, and *Railway*, would normally exhibit a dominant surface scattering mechanism. As a matter of fact, *Field 1* and *Field 2* correspond to two bare-soil fields, whereas *Railway* contains a railway. In Table V the percentage of pixels classified according to the three main Freeman-Durden classes is presented for the three analyzed zones, comparing the different methods. As shown in the tables, the

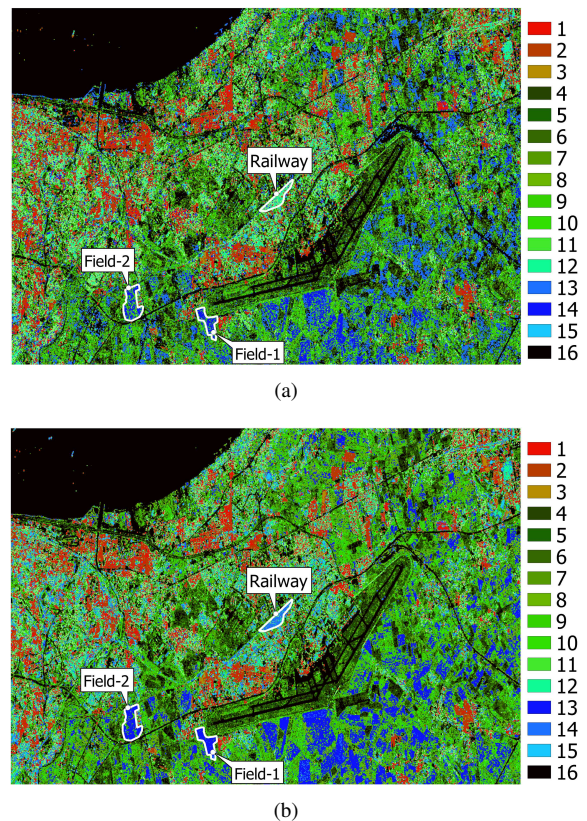


Figure 11: Freeman-Durden Wishart classification of the RADARSAT-2 data using  $K = 25$  looks. Subplots refer to a) sample coherence matrix (i.e., classical implementation), b) reconstructed matrix with the proposed method based on flip-flop.

proposed flip-flop based method significantly increases the percentage of pixels classified as surface scattering across all three zones. Specifically, for *Field 1*, the percentage of correctly classified pixels reaches 91.65%, compared to 68.23% with the classic method. A similar behavior is observed for *Field 2*. Interestingly, for the *Railway* zone, the new method classifies 65.94% of pixels as surface scattering, while reducing the double-bounce classification to just 0.30%.

## VII. CONCLUSIONS

In this paper, a new method for identifying covariance symmetries in multipass PolSAR images has been developed and examined. Precisely, the proposed algorithm exploits the temporal correlation available from repeated acquisitions to enhance the estimation of the polarimetric structure. Specifically, the covariance matrix of the data has been modelled as the Kronecker product between temporal (unstructured) and polarimetric (having some specific structures) covariances. The solution of the resulting constrained ML estimation problem has been obtained through the iterative alternating optimization flip-flop algorithm. Finally, some MOS criteria have been synthesized in order to properly select the structure of the polarimetric covariance matrix that provides the best representation of the scattering mechanism for a given pixel. The effec-

Table IV: Inferred scattering mechanism over urban area and agricultural fields.

area	method	$Z_1$	$Z_2$	$Z_3$	$Z_4$	$Z_5$	$Z_6$	$Z_7$	$Z_8$	$Z_9$
urban	classic	0.16%	0.30%	0%	14.38%	11.84%	4.12%	60.01%	3.60%	5.59%
	proposed	0.22%	0.55%	0%	17.45%	7.88%	1.99%	<b>68.2%</b>	1.35%	2.36%
agricultural	classic	0%	0.65%	0.28%	0%	7.78%	77.65%	0.08%	0%	13.56%
	proposed	0.01%	0.84%	<b>0.13%</b>	0.03%	1.01%	71.44%	0.01%	0.01%	<b>26.52%</b>

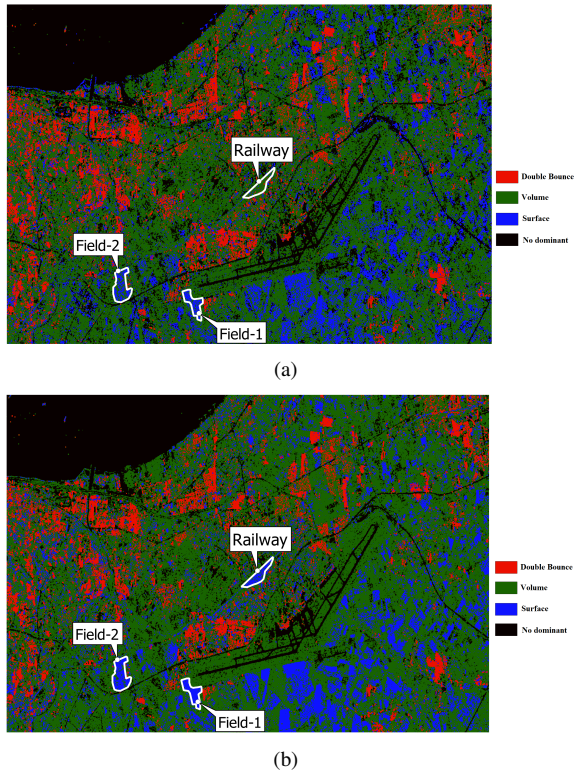


Figure 12: Inferred dominant scattering mechanisms over the RADARSAT-2 scene using different coherence matrix estimates. Subplots refer to a) sample coherence matrix (i.e., classical implementation), and b) reconstructed matrix with the proposed method based on flip-flop.

Table V: Inferred scattering mechanism over *Field-1*, *Field-2*, and *Railway* for the RADARSAT-2 image.

zone	method	surface	volume	double-bounce	no-dominant
<i>Field-1</i>	classic	68.23%	31.12%	0%	0.65%
	proposed	91.65%	8.19%	0%	0.16%
<i>Field-2</i>	classic	53.91%	44.94%	0.14%	1.01%
	proposed	77.10%	22.12%	0.13%	0.65%
<i>Railway</i>	classic	10.59%	81.30%	5.32%	2.79%
	proposed	65.94%	32.43%	0.30%	1.33%

tiveness of the proposed methodology has been proven by extensive simulations, demonstrating its advantages with respect to the competitor which does not exploit temporal correlations. Specifically, the proposed method is capable of reaching an accuracy of 94.6% for the reflection symmetry class and 92.0% for the azimuth class, in a typical simulated scenario, whereas the competitor obtain 72.5% and 72.6% for two classes, respectively, under the same simulation conditions. As a matter of fact, the Cohen's kappa coefficient achieved by

the proposed method is  $\kappa = 0.95$ , which significantly exceeds that of TUSML, where  $\kappa = 0.78$ . Moreover, tests conducted on measured X-band SAR data of RADARSAT-2 have shown its capabilities to enhance the image interpretation when it is plugged in widely used polarimetric decompositions. In particular, regarding the Freeman-Durden Wishart classification, tests have shown that the devised flip-flop based method significantly increases the percentage of correctly classified pixels. In fact, in zones dominated by surface scattering, it raises the percentage of correctly classified pixels from 68.23% with the classic method to 91.65%. Moreover, it also reduces the erroneously classified double-bounce pixels from 5.32% to just 0.30%. Interestingly, the analyses on the real SAR data have demonstrated the flexibility of the designed approach to be integrated into operational contexts and algorithms.

Future researches may consider the extension of this methodology to account for the presence of spatial heterogeneity within the data. Moreover, it could be of interest to consider some structures also on the temporal covariance (such as the Toeplitz structure [47]–[49]) to account for the statistical stationarity of the data acquisition mechanism.

## ACKNOWLEDGMENT

The authors would like to thank the Canadian Space Agency for supplying, as part of the SOAR program under the #1670 project, the polarimetric RADARSAT-2 data used in this paper.

## REFERENCES

- [1] A. Aubry, A. De Maio, and A. Farina, *Polarimetric Radar Signal Processing*, SciTech Publishing, Stevenage, UK, 2022.
- [2] G. Jin, A. Aubry, A. De Maio, R. Wang, and W. Wang, "Quasi-Orthogonal Waveforms for Ambiguity Suppression in Spaceborne Quad-Pol SAR," *IEEE Transactions on Geoscience and Remote Sensing*, vol. 60, pp. 1–17, 2022.
- [3] A. Freeman and S.L. Durden, "A Three-Component Scattering Model for Polarimetric SAR Data," *IEEE Transactions on Geoscience and Remote Sensing*, vol. 36, no. 3, pp. 963–973, 1998.
- [4] Y. Yamaguchi, T. Moriyama, M. Ishido, and H. Yamada, "Four-Component Scattering Model for Polarimetric SAR Image Decomposition," *IEEE Transactions on Geoscience and Remote Sensing*, vol. 43, no. 8, pp. 1699–1706, 2005.
- [5] Y. Yamaguchi, A. Sato, W. M. Boerner, R. Sato, and H. Yamada, "Four-Component Scattering Power Decomposition with Rotation of Coherency Matrix," *IEEE Transactions on Geoscience and Remote Sensing*, vol. 49, no. 6 part 2, pp. 2251–2258, 2011.
- [6] S. R. Cloude and E. Pottier, "An Entropy-Based Classification Scheme for Land Applications of Polarimetric SAR," *IEEE Trans. on Geoscience and Remote Sensing*, vol. 35, no. 1, pp. 68–78, January 1997.
- [7] J. S. Lee and E. Pottier, *Polarimetric Radar Imaging: From Basics to Applications*, CRC Press, 2009.
- [8] T. L. Ainsworth, Y. Wang, and J.-S. Lee, "Model-Based Polarimetric SAR Decomposition: An L1 Regularization Approach," *IEEE Transactions on Geoscience and Remote Sensing*, vol. 60, pp. 1–13, 2022.

- [9] T. Eltoft, L. Ferro-Famil, S. N. Anfinsen, and A. P. Doulgeris, "Polarimetric SAR Modelling: Mellin Kind Statistics and Time-Frequency Analysis," in *Mathematical Models for Remote Sensing Image Processing: Models and Methods for the Analysis of 2D Satellite and Aerial Images*, G. Moser and J. Zerubia, Eds., pp. 191–242. Springer International Publishing, Cham, 2018.
- [10] T. Eltoft and A. P. Doulgeris, "Model-Based Polarimetric Decomposition With Higher Order Statistics," *IEEE Geoscience and Remote Sensing Letters*, vol. 16, no. 6, pp. 992–996, 2019.
- [11] J. J. Van Zyl, "Unsupervised Classification of Scattering Behavior Using Radar Polarimetry Data," *IEEE Trans. on Geoscience and Remote Sensing*, vol. 27, no. 1, pp. 36–45, January 1989.
- [12] G. G. Lemoine, G. F. de Grandi, and A. J. Sieber, "Polarimetric Contrast Classification of Agricultural Fields using MAESTRO 1 AIRSAR Data," *International Journal of Remote Sensing*, vol. 15, no. 14, pp. 2851–2869, 1994.
- [13] L. Ferro-Famil, E. Pottier, and Jong-Sen Lee, "Unsupervised Classification of Multifrequency and Fully Polarimetric SAR Images based on the H/A/Alpha-Wishart Classifier," *IEEE Transactions on Geoscience and Remote Sensing*, vol. 39, no. 11, pp. 2332–2342, 2001.
- [14] J. S. Lee, K. P. Papathanassiou, I. Hajnsek, T. Mette, M. R. Grunes, T. Ainsworth, and L. Ferro-Famil, "Applying Polarimetric SAR Interferometric Data for Forest Classification," in *Proceedings. 2005 IEEE International Geoscience and Remote Sensing Symposium, 2005. IGARSS '05.*, 2005, vol. 7, pp. 4848–4851.
- [15] J.-S. Lee, M. R. Grunes, T. L. Ainsworth, L.-J. Du, D. L. Schuler, and S. R. Cloude, "Unsupervised Classification using Polarimetric Decomposition and the Complex Wishart Classifier," *IEEE Transactions on Geoscience and Remote Sensing*, vol. 37, no. 5, pp. 2249–2258, 1999.
- [16] S. E. Park, W. M. Moon, and E. Pottier, "Assessment of Scattering Mechanism of Polarimetric SAR Signal From Mountainous Forest Areas," *IEEE Trans. on Geoscience and Remote Sensing*, vol. 50, no. 11, pp. 4711–4719, 2012.
- [17] M. Dabboor and M. Shokr, "A New Likelihood Ratio for Supervised Classification of Fully Polarimetric SAR Data: An Application for Sea Ice Type Mapping," *ISPRS Journal of Photogrammetry and Remote Sensing*, vol. 84, pp. 1–11, 2013.
- [18] G. Di Martino, A. Iodice, and D. Riccio, "Closed-Form Anisotropic Polarimetric Two-Scale Model for Fast Evaluation of Sea Surface Backscattering," *IEEE Transactions on Geoscience and Remote Sensing*, vol. 57, no. 8, pp. 6182–6194, 2019.
- [19] Jong-Sen Lee, M.R. Grunes, E. Pottier, and L. Ferro-Famil, "Unsupervised Terrain Classification Preserving Polarimetric Scattering Characteristics," *IEEE Transactions on Geoscience and Remote Sensing*, vol. 42, no. 4, pp. 722–731, 2004.
- [20] Y. Lu, B. Zhang, and W. Perrie, "Arctic Sea Ice and Open Water Classification From Spaceborne Fully Polarimetric Synthetic Aperture Radar," *IEEE Transactions on Geoscience and Remote Sensing*, vol. 61, pp. 1–13, 2023.
- [21] Y. Wang and T. L. Ainsworth, "A Geometry-Compensated Sensitivity Study of Polarimetric Bistatic Scattering for Rough Surface Observation," *Remote Sensing*, vol. 16, no. 10, 2024.
- [22] Ze-Chen Li, Heng-Chao Li, Gui Gao, Wen Hong, and William J. Emery, "Unsupervised Classification for Multilook Polarimetric SAR Images via Double Dirichlet Process Mixture Model," *IEEE Transactions on Geoscience and Remote Sensing*, vol. 62, pp. 1–16, 2024.
- [23] S. V. Nghiem, S. H. Yueh, R. Kwok, and F. K. Li, "Symmetry Properties in Polarimetric Remote Sensing," *Radio Science*, vol. 27, no. 5, pp. 693–711, September-October 1992.
- [24] L. Pallotta, C. Clemente, A. De Maio, and J. J. Soraghan, "Detecting Covariance Symmetries in Polarimetric SAR Images," *IEEE Transactions on Geoscience and Remote Sensing*, vol. 55, no. 1, pp. 80–95, 2016.
- [25] L. Pallotta, C. Clemente, and A. De Maio, "Covariance Symmetries Classification in Polarimetric SAR Images," in *Polarimetric Radar Signal Processing*. Scitech Publishing, Stevenage, UK, 2022.
- [26] Y. Selén, *Model Selection*. Phd dissertation in electrical engineering, Uppsala University, Sweden, October 2004.
- [27] P. Stoica and Y. Selén, "Model-Order Selection: A Review of Information Criterion Rules," *IEEE Signal Processing Magazine*, vol. 21, no. 4, pp. 36–47, 2004.
- [28] P. Stoica, Y. Selén, and J. Li, "On Information Criteria and the Generalized Likelihood Ratio Test of Model Order Selection," *IEEE Signal Processing Letters*, vol. 11, no. 10, pp. 794–797, 2004.
- [29] S. M. Kay, "Exponentially Embedded Families-New Approaches to Model Order Estimation," *IEEE Trans. on Aerospace and Electronic Systems*, vol. 41, no. 1, pp. 333–345, January 2005.
- [30] S. M. Kay, *Fundamentals of Statistical Signal Processing: Estimation Theory*, vol. 1, Prentice Hall, 1993.
- [31] S. M. Kay, "The Multifamily Likelihood Ratio Test for Multiple Signal Model Detection," *IEEE Signal Processing Letters*, vol. 12, no. 5, pp. 369–371, May 2005.
- [32] L. Pallotta, A. De Maio, and D. Orlando, "A Robust Framework for Covariance Classification in Heterogeneous Polarimetric SAR Images and Its Application to L-Band Data," *IEEE Transactions on Geoscience and Remote Sensing*, vol. 57, no. 1, pp. 104–119, 2019.
- [33] L. Pallotta and M. Tesauro, "Screening Polarimetric SAR Data via Geometric Barycenters for Covariance Symmetry Classification," *IEEE Geoscience and Remote Sensing Letters*, vol. 20, pp. 1–5, 2023.
- [34] L. Pallotta and M. Tesauro, "Outlier Rejection by Means of Median Matrices for Polarimetric SAR Covariance Symmetry Classification," *IEEE Geoscience and Remote Sensing Letters*, vol. 20, pp. 1–5, 2023.
- [35] S. Han, Pia Addabbo, F. Biondi, C. Clemente, D. Orlando, and G. Ricci, "Innovative Solutions Based on the EM-Algorithm for Covariance Structure Detection and Classification in Polarimetric SAR Images," *IEEE Transactions on Aerospace and Electronic Systems*, vol. 59, no. 1, pp. 209–227, 2023.
- [36] K. Werner, M. Jansson, and P. Stoica, "On Estimation of Covariance Matrices with Kronecker Product Structure," *IEEE Transactions on Signal Processing*, vol. 56, no. 2, pp. 478–491, 2008.
- [37] A. Aubry, V. Carotenuto, A. De Maio, and L. Pallotta, "Assessing Reciprocity in Polarimetric SAR Data," *IEEE Geoscience and Remote Sensing Letters*, vol. 17, no. 1, pp. 87–91, 2019.
- [38] L. Pallotta, "Reciprocity Evaluation in Heterogeneous Polarimetric SAR Images," *IEEE Geoscience and Remote Sensing Letters*, vol. 19, pp. 1–5, 2020.
- [39] ESA, "PolSARPro (the Polarimetric SAR Data Processing and Educational Tool)," 2000-2019.
- [40] Lei Shi, Weidong Sun, Jie Yang, and Liangpei Zhang, "Polarimetric Calibration of Linear Dual-Pol SAR when Corner Reflectors are Unavailable," *ISPRS Journal of Photogrammetry and Remote Sensing*, vol. 214, pp. 209–230, 2024.
- [41] N. Cressie and C. K. Wikle, *Statistics for Spatio-Temporal Data*, John Wiley & Sons, 2011.
- [42] M. Razaviyayn, M. Hong, and Z.-Q. Luo, "A Unified Convergence Analysis of Block Successive Minimization Methods for Nonsmooth Optimization," *SIAM Journal on Optimization*, vol. 23, no. 2, pp. 1126–1153, 2013.
- [43] A. Aubry, A. De Maio, A. Zappone, M. Razaviyayn, and Z.-Q. Luo, "A New Sequential Optimization Procedure and Its Applications to Resource Allocation for Wireless Systems," *IEEE Transactions on Signal Processing*, vol. 66, no. 24, pp. 6518–6533, 2018.
- [44] Edward J. Hannan and Barry G. Quinn, "The Determination of the Order of an Autoregression," *Journal of the Royal Statistical Society: Series B (Methodological)*, vol. 41, no. 2, pp. 190–195, 1979.
- [45] Jacob Cohen, "A Coefficient of Agreement for Nominal Scales," *Educational and Psychological Measurement*, vol. 20, no. 1, pp. 37–46, 1960.
- [46] D. Hanis, K. Hadj-Rabah, A. Belhadj-Aissa, and L. Pallotta, "Dominant Scattering Mechanism Identification From Quad-Pol-SAR Data Analysis," *IEEE Journal of Selected Topics in Applied Earth Observations and Remote Sensing*, vol. 17, pp. 14408–14420, 2024.
- [47] X. Du, A. Aubry, A. De Maio, and G. Cui, "Toeplitz Structured Covariance Matrix Estimation for Radar Applications," *IEEE Signal Processing Letters*, vol. 27, pp. 595–599, 2020.
- [48] A. Aubry, P. Babu, A. De Maio, and R. Jyothi, "New Methods for MLE of Toeplitz Structured Covariance Matrices with Applications to RADAR Problems," *arXiv preprint arXiv:2110.12176*, 2021.
- [49] A. Aubry, P. Babu, A. De Maio, and R. Jyothi, "ATOM for MLE of Toeplitz Structured Covariance Matrices for RADAR Applications," in *2022 IEEE Radar Conference (RadarConf22)*, 2022, pp. 1–6.